Geophys. J. Int. (2009) **176,** 683–694 doi: 10.1111/j.1365-246X.2008.04000.x

Detectability and significance of 12 hr barometric tide in radon-222 signal, dripwater flow rate, air temperature and carbon dioxide concentration in an underground tunnel

Patrick Richon,[1,2] Frédéric Perrier,[3] Eric Pili[1] and Jean-Christophe Sabroux[4]

[1] *CEA, DAM, DIF,* F-91297 *Arpajon, France. E-mail: patrick.richon@cea.fr*
[2] *Institut de Physique du Globe de Paris, Équipe Géologie des Systèmes Volcaniques,* UMR-7154, 4 *place Jussieu,* F-75252 *Paris cedex* 05, *France*
[3] *Institut de Physique du Globe de Paris, Équipe de Géomagnétisme,* UMR-7154, *Université Paris Diderot,* 4 *place Jussieu,* F-75252 *Paris cedex* 05, *France*
[4] *Institut de Radioprotection et de Súreté Nucléaire, Centre de Saclay,* BP68, F-91192 *Gif-sur-Yvette, France*

Accepted 2008 October 9. Received 2008 October 8; in original form 2007 December 5

SUMMARY

Searching for small periodic signals, such as the 12 hr (S_2) barometric tide, and monitoring their amplitude as a function of time, can provide important clues on the complex processes affecting fluid transport in unsaturated fractured media under multiple influences. Here, first, we show that a modified spectrogram analysis (MSA) is more efficient than simple Fourier transform to reveal weak periodic signals. Secondly, we show how transient periodic signals can be monitored as a function of time using spectrograms. These methods are applied to time-series of radon and carbon dioxide concentration, dripwater flow rates and air temperature measured during several years in the Roselend dead-end tunnel, located in the French Alps near an artificial lake. A weak S_2 line is evidenced in radon concentration, with enhanced amplitude during transient radon bursts. Similarly, the S_2 line is observed using MSA in dripwater flow rates which sample mainly fracture flow, as suggested by a hydrochemical analysis, while it is not seen in dripwater flow rates sampling matrix flow. In the absence of a strong 24 hr line, the presence of a S_2 line suggests sensitivity to barometric pressure, and thus a significant advective contribution in radon and some dripwater transport. No S_2 line is observed in the carbon dioxide time-series. The temporal structure of the S_2 component, however, is not similar in the radon concentration and the dripwater flow rates, suggesting, in particular, that dripwater does not play a significant role in the generation of radon bursts. Temperature time-series exhibit a significant S_2 contribution, induced by atmospheric pressure, spatially organised in the tunnel, decreasing vertically upwards. A remarkable transient temperature inversion during radon bursts suggests that the additional advective air contributions responsible for the radon bursts occur from the non-saturated rocks below the tunnel.

Key words: Time series analysis; Fourier analysis; Tides and planetary waves; Permeability and porosity; Fractures and faults; Volcanic gases.

1 INTRODUCTION

Radon-222, a radioactive inert gas of half-life 3.8 d, is released into the pore space from rock minerals bearing traces of radium-226. It can be transported through groundwater or air into the open atmosphere (Tanner 1964; Nazaroff 1992). Radon-222 is important to study because it represents more than half the radiation dose to the general population (Porstendörfer 1996), and can be present at exceptional concentrations in poorly ventilated dwellings in some geological areas (Ielsch *et al.* 2001). In addition, radon can be used to characterize geodynamical and environmental processes. Radon emanation and transport indeed may be affected by geodynamical processes such as volcanic activity (Baubron *et al.* 1991; Cigolini *et al.* 2005) and earthquakes. Radon-222 concentration anomalies before large earthquakes have been reported in the soil (Richon *et al.* 2003), groundwater (Virk & Singh 1994; Igarashi *et al.* 1995), open air (Yasuoka & Shinogi 1997), domestic basements (Crockett *et al.* 2006a) and underground tunnels (Yamauchi & Shimo 1982). While, on the one hand, such anomalies remain isolated observations, not supported by a detailed theoretical understanding, on the other hand, radon emission has been observed in laboratory experiments in association with rock deformation (Holub & Brady 1981; King & Guangwei 1990). In a natural system, such radon production processes could be combined, with efficient transport modes. Studying the properties of geophysical systems with respect to transport of radon, therefore, appears as a major practical and fundamental scientific issue.

The release and transport of radon in saturated and unsaturated natural media can be of diffusive nature (Lehmann *et al.* 2000), but can be dramatically modified by advective transport. In particular, radon concentration was observed to be affected by atmospheric pressure variations in the soil (Pohl-Rüling & Pohl 1969; Clements & Wilkening 1974) or in underground settings (Perrier *et al.* 2004). Conversely, the sensitivity of radon to atmospheric pressure variations can be used to monitor the soil transport properties as a function of time (Pinault & Baubron 1997). Atmospheric pressure variations are characterized by a strong 12 hr (S_2) wave (Simpson 1919), with a definite spatial variation. This S_2 wave is primarily due to the solar heating of the atmosphere, and is referred to as barometric tide; it should not be confused with the gravitational lunar semidiurnal M_2 tide which has a period of 12.42 hr. In a first approximation, the amplitude of the atmospheric S_2 wave is locally homogeneous and its variation with the latitude Φ is given by 1.2 hPa $\times$ $\cos^3\Phi$ (Haurwitz 1956; Haurwitz & Cowley 1973). A corresponding S_2 signal is observed in the power spectrum of radon concentration and, for example, has been reported on the Taal volcano (Richon *et al.* 2003) or in underground settings (Martín-Luis *et al.* 2002; Unger *et al.* 2004). In such cases, the S_2 signal emerges while the diurnal 24 hr (S_1) line is not observed (S_2 amplitude $\gg$ S_1 amplitude). This strongly suggests a barometric effect. Sometimes the S_2 wave is not observed in power spectra (Perrier *et al.* 2007), which may indicate that the atmospheric pressure sensitivity might be absent or that it cannot be observed given the limitations of the instrumental or data analysis methods.

In this paper, we present methods to exhibit the S_2 barometric wave in time-series and to monitor its amplitude as a function of time. These methods are then applied to time-series of radon concentration, dripwater flow rate, carbon dioxide concentration, and temperature recorded in the dead-end Roselend tunnel. This tunnel is characterized by a low radon background level of about 800 Bq m^{-3} and by transient bursts, reaching up to 65 600 Bq m^{-3} with a duration of up to several weeks (Perrier *et al.* 2005b; Richon *et al.* 2004). These bursts, poorly understood at the moment, could result from hydrogeological effects or deformation events associated with the variations of water level in the nearby artificial Roselend Lake (Trique *et al.* 1999). We will use the obtained results to discuss how the search and monitoring of the S_2 wave can provide clues on the properties of the varying host rock and, in particular, the generation of the radon bursts.

2 SIGNAL PROCESSING METHODS

2.1 Principle

We developed a tool to extract periodicities, in the range of the diurnal or semidiurnal variations that can remain hidden in noise in a simple Fourier spectrum. We have also used classical spectrograms as a function of time to study the temporal variations of these clearly identified periodic signals. This modified spectrogram analysis (MSA) is inspired in part by the Wiener–Kinchin theorem: the Fourier transform of the autocorrelation function of a signal is the power spectrum of the signal (Khinchin 1949), and, in part, by a recent and innovative statistical analysis of radon time-series (Crockett *et al.* 2006b).

2.2 Implementation

We first describe our methods using a simple synthetic signal of radon concentration displayed as signal 1 in Fig. 1(a). This signal includes a yearly variation with a 2000 Bq m^{-3} peak to peak amplitude, Gaussian noise with root mean square (rms) value of 100 Bq m^{-3} and periodic signals with periods 15, 18 and 25 hr and peak to peak amplitudes 640, 80 and 640 Bq m^{-3}, respectively. While the 18 hr signal is present over the whole time-series (red segment in Fig. 1a), the 15 and 25 hr signals (green and blue segment in Fig. 1a) are only present over a 200 days duration.

First, to remove long-term variations and large anomalies (Fig. 1a), we apply a derivative operation (Fig. 1c). The basic derivative function from DADisp^{TM} software package is used. This function calculates the derivative of evenly spaced data by taking points (n), ($n-1$) and ($n+1$), finding the quadratic curve fitting these three points. The slope of this fitted curve at point (n) defines the derivative of point (n).

In a second stage, an autocorrelation function (Fig. 1e) is calculated on the derivative. The autocorrelation function (Box & Jenkins 1976) can be used for the following two purposes: first, to detect non-randomness in data and, second, to identify an appropriate time-series model if the data are not random. Given measurements, Y_1, $Y_2, \ldots, Y_N$ at time $X_1, X_2, \ldots, X_N$, the lag k autocorrelation function is defined as:

$$\Gamma_k = \frac{\sum_{i=1}^{N-k} (Y_i - \bar{Y})(Y_{i+k} - \bar{Y})}{\sum_{i=1}^{N} \left(Y_i - \bar{Y}\right)^2}. \quad (1)$$

Although the time variable, X, is not used in the formula for autocorrelation, the assumption is that the observations are equispaced. Autocorrelation is a correlation coefficient. However, instead of a correlation between two different variables, the correlation is between two values of the same variable at times X_i and X_{i+k}. The autocorrelation function is symmetric with respect to positive and negative time lags. This operation extracts and amplifies periodic signals, if existing, and eliminates non-periodic signals, considered as white noise (Olvera 2005).

Finally, on the resulting positive part (on X-axis) of the autocorrelation function (Fig. 1e), we apply a spectrogram display using a regular Fast Fourier Transform FFT (on 2048 hr with Hamming windowing) computed with sliding windows of 400 hr and an overlap of 398 hr (Fig. 1f). Note that periodicities emerge as line only in the Fourier spectra, and not as a function of chronological time or time lag, which replaces chronological time in the autocorrelation function. The horizontal axis of our spectrograms represents time, the vertical axis is frequency, and the intensity of each point in the image represents the amplitude of a particular frequency at a particular time. The spectrogram is the result of calculating the frequency spectrum of windowed frames of a compound signal. It is a 3-D plot of the energy of the frequency content of a signal as it changes over time. In the Fig. 1(b), the periodicities emerge clearly as a function of time.

Now we have introduced our basic tools: a modified spectrogram (MSA, Fig. 1f) to extract the periodicities, and a regular spectrogram to represent the presence of periodicities as a function of time (spectrogram Fig. 1d). In the next section, we apply our signal processing tool (MSA) to another synthetic signal, representing better a natural radon signal, in order to show the efficiency of this method.

2.3 Validation

This second simulated signal 2 in Fig. 1(g) includes a background signal made of three components: a Gaussian white noise of 100 Bq m^{-3} standard deviation, a yearly variation with a peak to

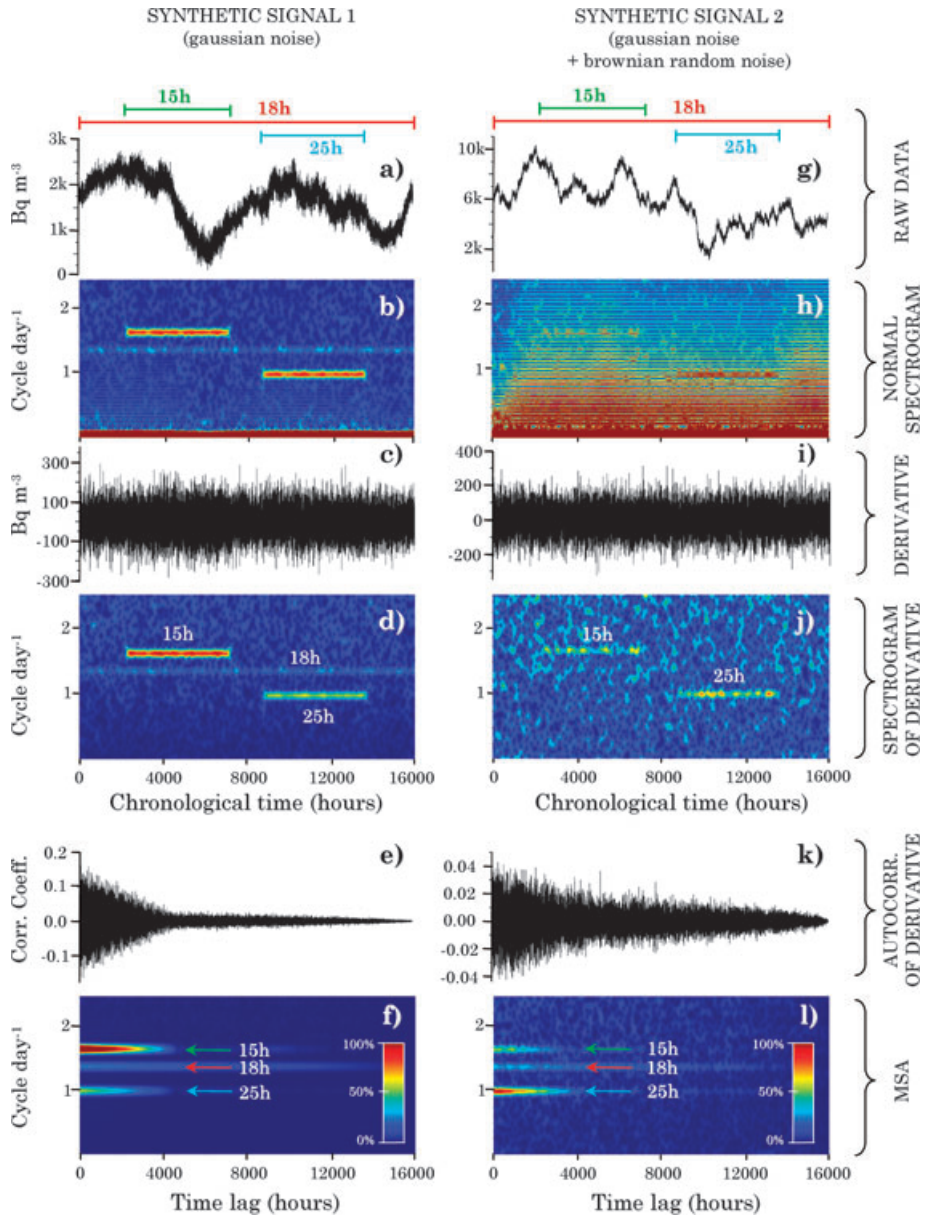

Figure 1. Modified Spectrogram Analysis (MSA) protocol (a–f and g–l) applied on two different hourly synthetic signals: synthetic signal 1 (a), containing random noise, yearly variation and three frequencies (15, 18 and 25 hr) plus an annual cycle and synthetic signal 2 (g) containing a Brownian and Gaussian white noise, three frequencies (15, 18 and 25 hr) plus an annual cycle.

peak amplitude 1000 Bq m^{-3}, and a Brownian random walk signal. This Brownian noise is generated, at every sampling time, by a step of +40 or –40 Bq m^{-3}, randomly chosen. This signal mimics rather well radon concentration signals, for example in the soil or the atmosphere of underground quarries (Perrier *et al.* 2004). On top of this background signal, we have added three sinusoidal signals: one oscillation with a period of 18 hr (red segment in Fig. 1g), with peak to peak amplitude of 40 Bq m^{-3}; one oscillation with a period of 15 hr (green segment in Fig. 1g), with peak to peak amplitude of 80 Bq m^{-3}, present only during a 200 d period; and one oscillation with a period of 25 hr (blue segment in Fig. 1g), with peak to peak amplitude of 160 Bq m^{-3}, present only during a 200 d period, as indicated in Fig. 1(g).

In this case, 15, 18 or 25 hr peaks cannot be clearly identified in the normal spectrogram (Fig. 1h). A continuous frequency corresponding to a period of 18 hr does not emerge in the spectrogram (Fig. 1j) after derivative operation (Fig. 1i) but two horizontal segments at 15 and 25 hr appear clearly. By contrast, 15, 18 and 25 hr signatures emerge remarkably in the MSA (Fig. 1l). This illustrates the ability of this sequence of treatments to reveal hidden periodic signals. The MSA, using derivative (Fig. 1i) and autocorrelation functions (Fig. 1k) is clearly more efficient than a classical FFT spectrum or standard spectrogram (Fig. 1h) applied on a raw time-series.

3 DATA SET AND EXPERIMENTAL METHODS

3.1 Site

The dead-end Roselend tunnel is located in the west bank of the artificial Roselend Lake (French Alps) at an average altitude of 1577 m

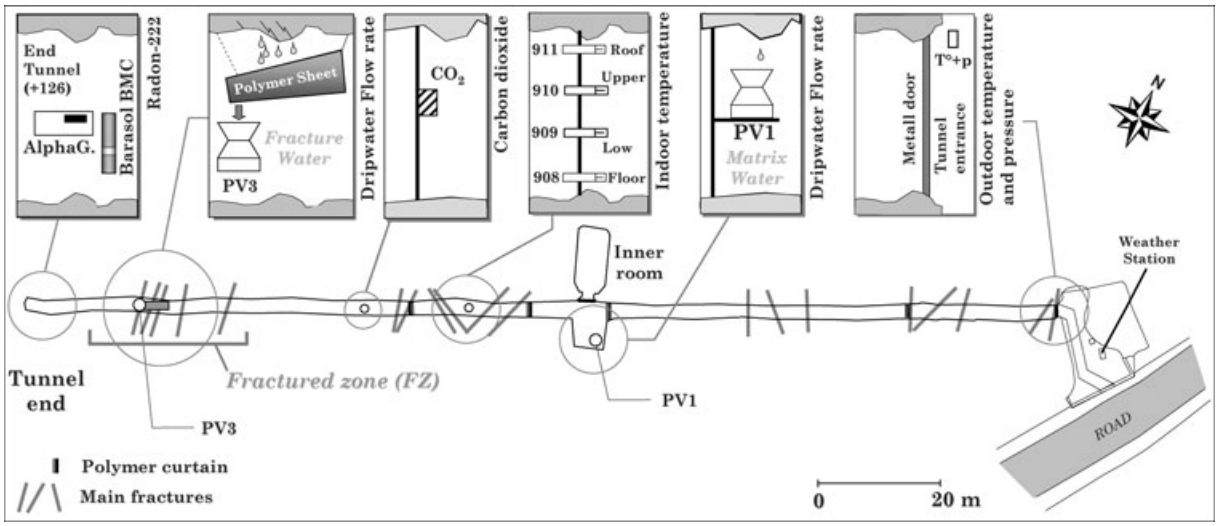

Figure 2. Horizontal layout of the Roselend tunnel showing the locations of the radon-222 monitoring points, instrumented with BMC and AlphaGUARD^{TM} devices from 2001 to 2006, inset show vertical sections depicting the local installation of sensors. Locations of the dripwater flow rate: rain gauge PV1 (matrix water) and PV3 (fracture water, under Fractured Zone FZ). Precise air tunnel temperature profile measurements in the middle of the tunnel.

above sea level, at a mean distance of about 600 m from the Roselend dam. This tunnel has been described previously (Patriarche *et al.* 2007; Provost *et al.* 2004; Richon *et al.* 2004). It is hosted in fractured gneiss, granites and micaschists. It has an irregular section with an average dimension of 1.8 m × 2 m and a length of 128 m, total volume and wall surface area are estimated to be about 496 m^3 and 1250 m^2, respectively (Fig. 2). This tunnel was instrumented in 1995 to study the relationship between radon concentration and deformation induced by the level variation of the nearby artificial Roselend Lake (Trique *et al.* 1999). In this paper, we use data from an expanded set of instruments installed since 2002 (Provost *et al.* 2004).

3.2 Experimental setup

Two different types of instruments are used to monitor the radon concentration in the atmosphere at the end of the tunnel, 126 m from the entrance (Fig. 2). AlphaGUARD^{TM}, manufactured by *Genitron GmbH* (Ruckerbauer & Winkler 2001), is an ionisation chamber of 0.5 L located behind a diffusion barrier (fibre filter paper) that has a characteristic time of 20 min for radon and thus eliminates radon-220 which has a half-life of 55.6 s. This chamber is polarized by a high voltage potential (+500 V). Electrons produced in the chamber volume by alpha disintegrations in air (electron avalanche and pulse mode) are collected at a central electrode. The least count sensitivity is 3 Bq m^{-3}. The probe is equipped with an internal temperature sensor (±0.2 °C), an atmospheric pressure sensor (±0.1 hPa) and a humidity sensor (±1 per cent RH).

The Barasol^{TM} (BMC), manufactured by *Algade* (Ruckerbauer & Winkler 2001; Papastefanou 2002), is based on the detection of alpha particles by a silicon junction in a chamber. As for AlphaGUARD^{TM}, a diffusion barrier (fibre filter paper) with a characteristic diffusion time of 20 min eliminates the contribution of radon-220. Discrimination from short-lived decay products of radon-222 deposited on the silicon junction is performed by an energy window from 0.1 to 6.1 MeV. The sensitivity of the BMC probe is given by a least count sensitivity of 1 count hr^{-1}, corresponding to an air concentration of about 50 Bq m^{-3}. The probe is equipped with an internal temperature sensor (±0.2 °C) and an atmospheric pressure sensor (±0.5 hPa).

Water is dripping from the roof of the tunnel. Dripwater flow rates were measured as a function of time in two different settings (Fig. 2). PV1, at 57 m from the tunnel entrance, provides matrix water from one single outlet, collected into a rain gauge. PV3, at 115 m from the entrance, provides fracture water contributed from several outlets in a fractured zone FZ (Pili *et al.* 2004) and collected in a 3 × 2 m^2 polymer sheet. The residence time is long for matrix water (PV1), typically of 3–12 months (Pili *et al.* 2008), while it is short for fracture water (PV3), about 0.5–3 months. Fracture flow is due to percolation of surface water through fracture network mostly at unsaturated conditions (Patriarche *et al.* 2007). Matrix water probably occurs under saturated conditions and is not directly connected to the surface.

A vertical temperature profile in the atmosphere is recorded at a distance of 74 m from the tunnel entrance (Fig. 2), using four autonomous Seabird^{TM} probes with an absolute accuracy of ±2 10^{-3} °C and a sensitivity of 10^{-4} °C. Carbon dioxide concentration in the atmosphere is measured at 95 m from the entrance with an *aSENSE^{TM}* (*Sensair*) probe using a non-dispersive infrared technology. Its accuracy is 3 per cent in the 0–5000 ppm range.

3.3 Time-series

Hourly data (for CO_2, temperature, pressure, flow rate and radon) and daily data (lake level) used in the present paper cover the period from 2002 June to 2006 June (Fig. 3). Radon concentration in the tunnel atmosphere, measured by BMC and, for a shorter time period, with AlphaGUARD^{TM} is shown as a function of time (Fig. 2), together with flow rates in PV1 (matrix water) and PV3 (fracture water), air temperature in the tunnel, atmospheric pressure and outdoor air temperature. In addition, carbon dioxide concentration has been measured since 2004 November. While the measurement of radon concentration C_{Rn}^{BMC} with the BMC sensor is continuous during the entire 4 yr period, the radon concentration C_{Rn}^{A} measured with AlphaGUARD^{TM} was interrupted in 2003 July, for a duration of 1.5 months, because of a power failure. This did

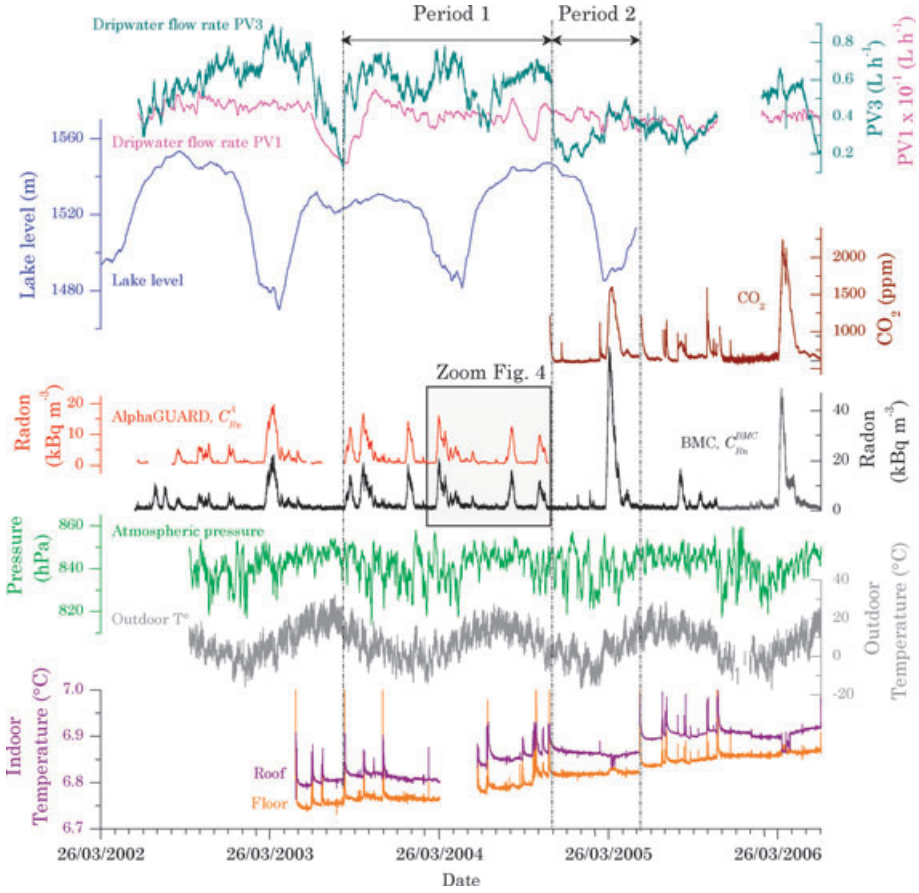

Figure 3. Time-series of parameters measured from 2002 June to 2006 June: dripwater matrix water flow rate PV1 (57 m) and fracture water PV3 (115 m). Radon-222 measured at 126 m with BMC and with AlphaGUARD^{TM} device. Atmospheric pressure measured in tunnel with the BMC device and CO_2 concentration acquired at 95 m. Daily lake level performed by EDF. External temperature measured by a weather station near the tunnel entrance and precise temperature profile in the tunnel measured at 74 m and at 10 cm from the roof and 10 cm from the floor. The two periods (1 and 2) statistically analysed in this paper are indicated by the vertical dot lines.

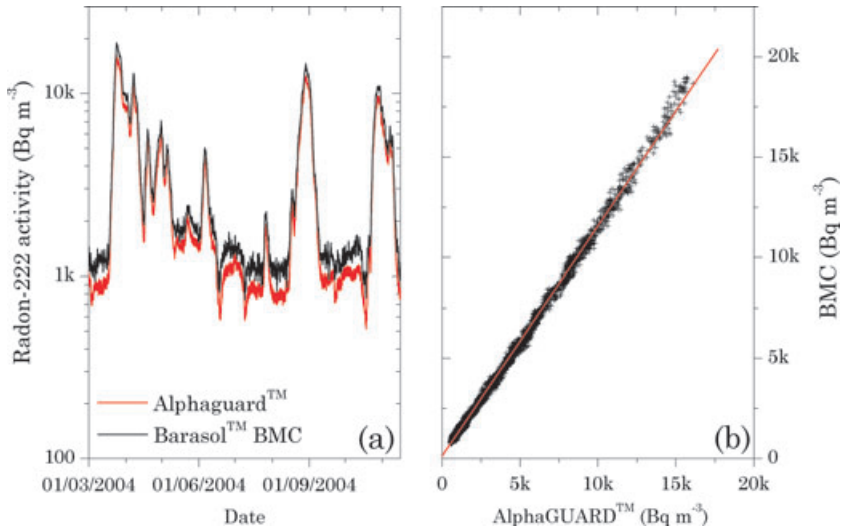

Figure 4. Calibration and sensitivity comparison between radon concentrations measured by AlphaGUARD^{TM} (C^{A}_{Rn}) and BMC (C^{BMC}_{Rn}) in the Roselend tunnel: comparison between time-series (a) and BMC versus AlphaGUARD^{TM} (b).

not affect the autonomous BMC and the other sensors connected to batteries. The AlphaGUARD^{TM} was removed from the tunnel in 2004 November. The two measurements of radon concentration are remarkably similar, despite a larger statistical noise on C^{BMC}_{Rn}. Comparison between C^{BMC}_{Rn} and C^{A}_{Rn} is shown in Fig. 4(a) for a subinterval as a function of time, and C^{BMC}_{Rn} is shown versus C^{A}_{Rn} in Fig. 4(b). Radon background level ranges from 800 to 1200 Bq m^{-3}, with bursts reaching an amplitude of 65.6 kBq m^{-3} in 2005 March.

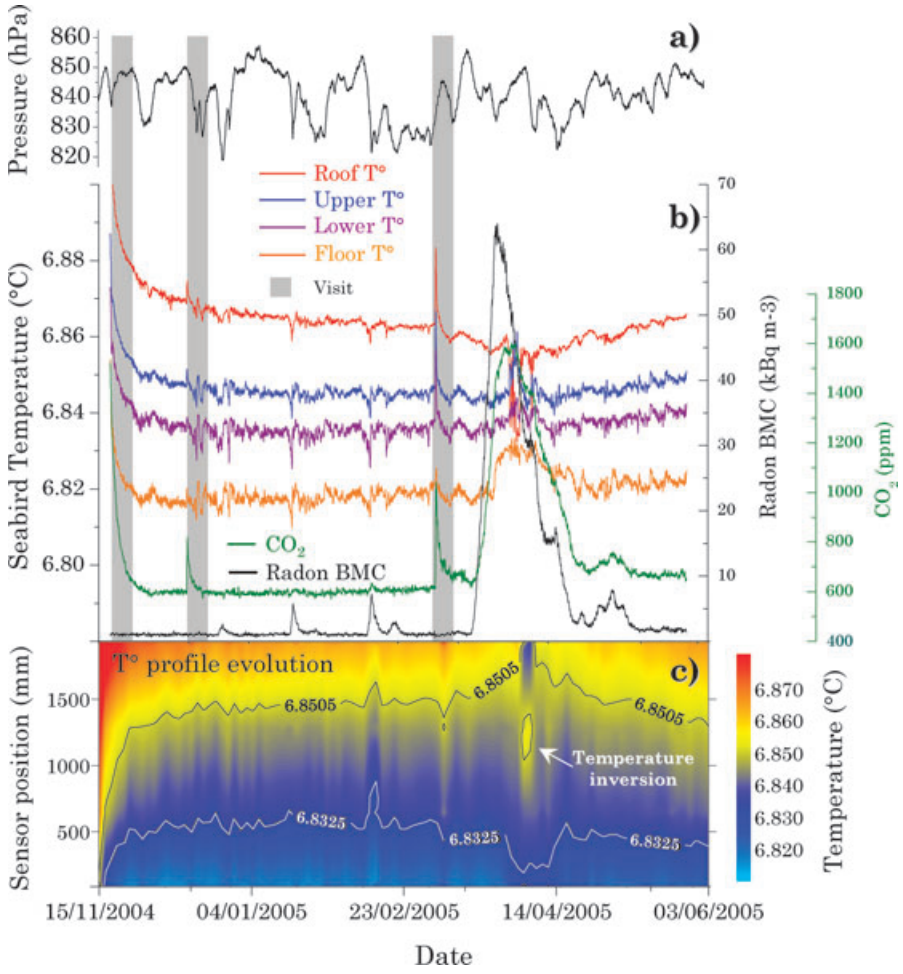

Figure 5. Zoom during Period 2 on highest radon (65.6 kBq m^{-3}, black curve) and CO_2 anomalies (1620 ppm, green curve) produced in 2005 April 3 (b) and correlated with the external forcing induced by the filling up of the artificial lake (Fig. 3). Anomalies are not correlated with the atmospheric pressure (a), but another clear correlation is detected on vertical temperature profile measured in the middle of the tunnel. This temperature event (c) is characterized by the decrease of the top temperature (–0.023°C, red curve) and by the increase of the bottom temperature (+0.015°C, orange curve).

This behaviour was already reported (Trique *et al.* 1999; Richon *et al.* 2004), but with smaller maximum burst amplitudes. The two largest radon bursts, observed in March 2005 and in 2006 March (Fig. 3), are also associated with a burst in carbon dioxide concentration and with a temperature inversion (Fig. 5c). These events occur after rapid reloading of the lake level. The dripwater flow rates do not show such strong variations, and remain within ±50 per cent of the average, except during the summer drought of 2003 August.

While the outside temperature has a yearly cycle from about –10 to +25 °C, the temperature in the tunnel atmosphere shows only small variations from 6.75 to 6.90 °C. Spikes followed by an exponential relaxation are due to human presence in the tunnel. In addition, a small yearly variation of about 0.02 °C peak-to-peak is observed on top of a linear temperature rise of 0.039 °C per year. Although this linear increase could be a result of global warming as detected in other underground sites (Perrier *et al.* 2005a), it most probably results here from heating contribution from instruments, AC/DC transformer, chargers and batteries present in the tunnel.

Temperature recorded at four different vertical positions in the tunnel are also shown in Figs 5(b) and (c). These temperature signals are dominated by effects induced by atmospheric pressure (Fig. 5a) variations (Perrier *et al.* 2001). Human presence (grey vertical bar in Fig. 5b) in the tunnel also leaves a clear positive signature on the temperature records, especially near the roof, as commonly observed (Crouzeix *et al.* 2006). Most of the time the temperature shows a normal vertical stratification in the tunnel, that is, relatively hot air is found near the roof. This stratification is probably due to the heat sources scattered in the tunnel (Crouzeix *et al.* 2006).

During the large radon burst, however, a reverse thermal stratification is produced and maintained during 5 d before 2005 April 14 (Fig. 5c). The radon burst thus also contains a subevent of peculiar thermal inversion, 5 d after the maximum of carbon dioxide. Temperature differences here are smaller than 0.06 °C and the effects could only be observed because of the high sensitivity of the Seabird™ sensors. During the large radon burst, the temperature signal is a decrease near the roof (red curve in Fig. 5b), and an increase near the floor (orange curve in Fig. 5b).

In addition, we point out that, in contrast to carbon dioxide and temperature, radon concentration is not at all affected by human presence in the tunnel. This implies that radon concentration must be vertically homogeneous in the tunnel. This was confirmed by dedicated measurements using two AlphaGUARD™ sensors installed temporarily at the location of the temperature profile. A homogeneous radon-222 concentration is in fact expected, given the value of the diffusion length of radon-222 in air (2 m).

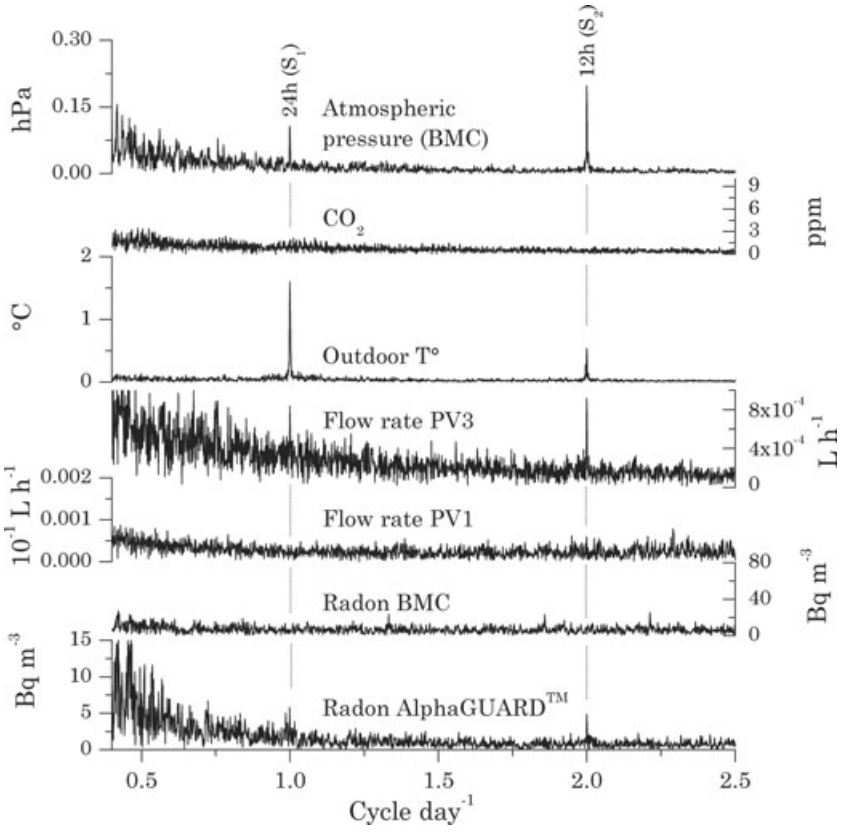

Figure 6. Amplitude spectra during Period 1 versus frequency, expressed in cycle per day for the atmospheric pressure, CO_2 concentration, outdoor T°, dripwater flow rate at PV3 (fracture water) and PV1 (matrix water) and radon concentration measured by AlphaGUARD™ and BMC.

Let us now concentrate on time Period 2 (Fig. 3), during which carbon dioxide concentration and temperature records in the atmosphere of the tunnel are available. During this period, a particularly strong radon burst, with a peak concentration of 65.6×10^3 Bq m^{-3}, is observed after smaller bursts. Note that a burst of carbon dioxide occurs simultaneously with a peak concentration of 1620 ppm reached 5 d after the peak of the radon concentration (Fig. 5b). Note also that, while radon concentration has a steep increase at the beginning of the burst, the carbon dioxide has a relatively gently rising slope. Three perturbations followed by an exponential relaxation, seen on this carbon dioxide record, actually correspond to human presence in the tunnel. The smaller radon bursts from 2004 December to 2005 February are also associated with small, but nevertheless visible, signals in the carbon dioxide concentration.

These various time-series contain a large amount of information that needs to be deciphered to reveal the underlying physical process. In the following, we concentrate on the periodic signals with periods from about 5 hr to 2 days. This range is important because of the large diurnal and semidiurnal forcing, as can be shown using the Fourier amplitude spectrum shown in Fig. 6. In this figure, we have used a time section of 441 d from 2003 September 1 to 2004 November 16, shown as Period 1 in Fig. 3. The S_1 and S_2 lines are visible in the atmospheric pressure and outdoor temperature spectra. In the atmospheric pressure spectrum, as already mentioned in the introduction, the S_2 line is significantly larger than the S_1 line. The amplitude of the S_2 barometric tide is observed to be 0.2 hPa, and is in the regular range at this latitude (46° North) and altitude, 1577 m a.s.l. (Arabelos *et al.* 1997; Ray 2001).

By contrast, the S_1 line dominates in the outdoor temperature spectrum (Fig. 6). Clear S_1 and S_2 lines are also observed in the dripwater (fracture water PV3) flow rate, with larger amplitude for S_2 compared with S_1. This may indicate that this water dripping is sensitive to atmospheric pressure which is the most obvious available forcing with a strong S_2 line. A similar correlation between fracture flow rate and atmospheric pressure has been reported in a cave (Genty & Deflandre 1998). No clear S_1 and S_2 lines are observed in the other power spectra, but these lines are barely visible above noise in the C_{Rn}^{A} power spectrum. This may be due to the fact that the S_1 and S_2 lines are not present or that a Fourier amplitude spectrum is not efficient to assess the presence of such periodic signals. Therefore, in the next section, we apply MSA, designed to enhance the signal over noise ratio of a periodic signal in this frequency range, on these time-series.

In the temperature time-series, the short term variations, resembling high frequency white noise, are actually the response at 12 hr. The intensity of the S_2 line is shown in Fig. 7 as a function of vertical position. The thermal S_2 response in the atmosphere of the tunnel is smoothly decreasing from floor to roof.

4 APPLICATION OF THE DATA PROCESSING METHODS TO DATA FROM THE ROSELEND TUNNEL

4.1 Detectability of small periodic signals

The process of the MSA is shown in Fig. 8 for the C_{Rn}^{A} time-series in Period 1. The spectrogram computed for this radon time-series

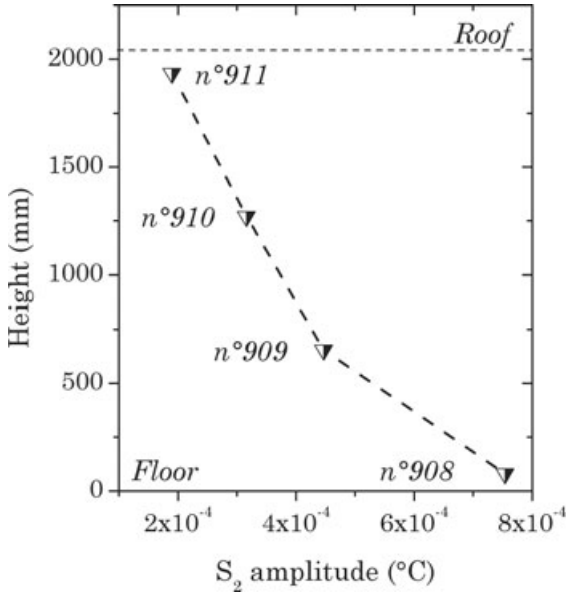

Figure 7. S_2 amplitudes in temperature signals (FFT) reported versus vertical position for four highly sensitive temperature devices in the tunnel atmosphere.

(Fig. 8a) is shown in Fig. 8(b). No clear accumulation of energy is shown as a function of time and frequency. The periodic signals remain hidden in the large dynamic variations of the signal. The spectrogram computed using the derivative (Fig. 8c), shown in Fig. 8(d) as a function of time, is less affected by the long period noise, and localization energy concentrations referred to as hotspots in this paper, close to 100 per cent energy of signal, can be distinguished at 12 hr period. In the resulting MSA displayed in Fig. 8(f), a clear component at 12 hr is now identified, with a weaker harmonic at 24 hr. The spectrogram Fig. 8(b) demonstrates that it is necessary to apply a derivative operation on raw data to suppress low frequencies. A second spectrogram (Fig. 8d) is calculated after a single derivative operation on C_{Rn}^{A}, and it is shown as a function of chronological time. In Fig. 8(e), the autocorrelation is shown as a function of time lag. In MSA, (Fig. 8f) shows a marked horizontal line at 2 cycles per day, corresponding to the S_2 wave. A smaller line at 1 cycle per day is also visible in this spectrogram. The simple FFT spectrum is shown in Fig. 8(g) while the FFT spectrum performed on the signal at the end of our analysis is shown in Fig. 8(h). The S_1 and S_2 lines appear much more remarkably in Fig. 8(f) than in Figs 8(b) and (d). To test the MSA process with real data, a synthetic periodic signal with a period of 15 hr and a peak-to-peak amplitude of 10 Bq m^{-3} has been added to the real data time-series. No peak at 15 hr can be clearly identified, neither in the FFT of Fig. 8(g) nor in other spectrogram of Figs 8(b) and (d). By contrast, it emerges remarkably in the MSA (Fig. 8f) and in its FFT spectrum (Fig. 8h).

Once the MSA has been performed, we can assess the frequency content of the signal with a reasonable reliability. Periodicities at 12, 24 (real) and 15 hr (synthetic) are seen in Fig. 8(f). Using this information, the normal spectrogram Fig. 8(d) can be re-examined. Now, we can infer that most hotspots in Fig. 8(d) are artefacts, except those at the clearly identified periodicities in Fig. 8(f), and it is possible to claim that there seems to be a correlation between content of S_2 wave (hotspots) and occurrence of the radon bursts. This figure shows that periodic signals are not present all the time in the radon concentration, but are strongly modulated as a function of time, with stronger amplitude during bursts. Note that a line at 12.42 hr (or 1.932 cycles per day, Earth tide M_2) is not observed. Our sensitivity study indicates that the M_2 peak to peak amplitude, if present in the radon signal, must be smaller than 2 Bq m^{-3}.

Once the basic periodicities of the radon signal have been assessed, it is interesting to study simultaneously radon concentration and other transport properties of the system. In the following, we first consider radon concentration and flow rates, then carbon dioxide and temperature.

4.2 Application to radon and flow rate time-series

In Fig. 9, we concentrate on simultaneous time-series during Period 1: C_{Rn}^{A} and C_{Rn}^{BMC}, dripwater flow rate of matrix water, of fracture water, and atmospheric pressure. Also C_{Rn}^{BMC} and fracture water, which are recalled in Fig. 9(a). Spectrograms of the time derivative of the signals and of the corresponding MSA are shown as a function of chronological time and time lag in Figs 9(b) and (c), respectively. The S_1 and S_2 lines appear clearly in the MSA of atmospheric pressure (Fig. 9c). The normal spectrogram (Fig. 9b) also shows these two lines, but their intensity varies as a function of time. For C_{Rn}^{A}, the S_2 line, and possibly the S_1 line, appears with the MSA, as already discussed previously. By contrast, no S_2 line is observed for C_{Rn}^{BMC}, neither in the MSA nor in the classical spectrogram, which now confirms the first indication from amplitude spectra shown in Fig. 6. In the dripwater flow rate of fracture water, the S_2 line, already identified using the Fourier amplitude spectra (Fig. 6), emerges clearly from the MSA (Fig. 9c). The time variation of this clearly identified periodicity is given in Fig. 9(b). The time structure in the fracture water signal appears quite different from C_{Rn}^{A}.

4.3 Application to radon, CO_2 and temperature time-series

We now turn to the MSA of the signals during Period 2. Only the BMC sensor was available (Fig. 10a) and S_2 and S_1 lines are not observed in the MSA (Fig. 10c). In the normal spectrogram as a function of time (Fig. 10b), a S_2 hotspot is observed during the large radon burst, at the maximum of carbon dioxide, but not at the maximum of the radon burst itself. This may provide an interesting clue on the underlying mechanism. S_2 or S_1 lines are not observed for the carbon dioxide, whereas the S_2 line is present in the fracture water signal, both with the MSA or with the spectrogram as a function of time (Figs 10b and c). The S_2 line also appears clearly in the MSA of the temperature time-series, especially near the floor, as noticed before. The MSA thus confirms the presence of the S_2 periodicity in the temperature time-series, which was already known from the Fourier spectra (Fig. 7). However, the MSA reveals that the S_1 periodicity in the temperature time-series is very small, below detection level. This shows that daily modulation of natural ventilation in the tunnel is very small, in contrast to the situation in a tunnel in Nepal (Perrier *et al.* 2007), where the daily modulation of temperature can be observed at 78 m distance from the entrance.

5 DISCUSSION

Using the MSA method presented in this paper, we have shown that S_1 and S_2 periodicities of the radon concentration can be evidenced using an AlphaGUARD^{TM} sensor, but not with the BMC sensor, which records the other features of the radon signal. Note that a larger amplitude of the S_2 line would be recorded by the BMC, sensor. It is a coincidental feature of the Roselend tunnel that the

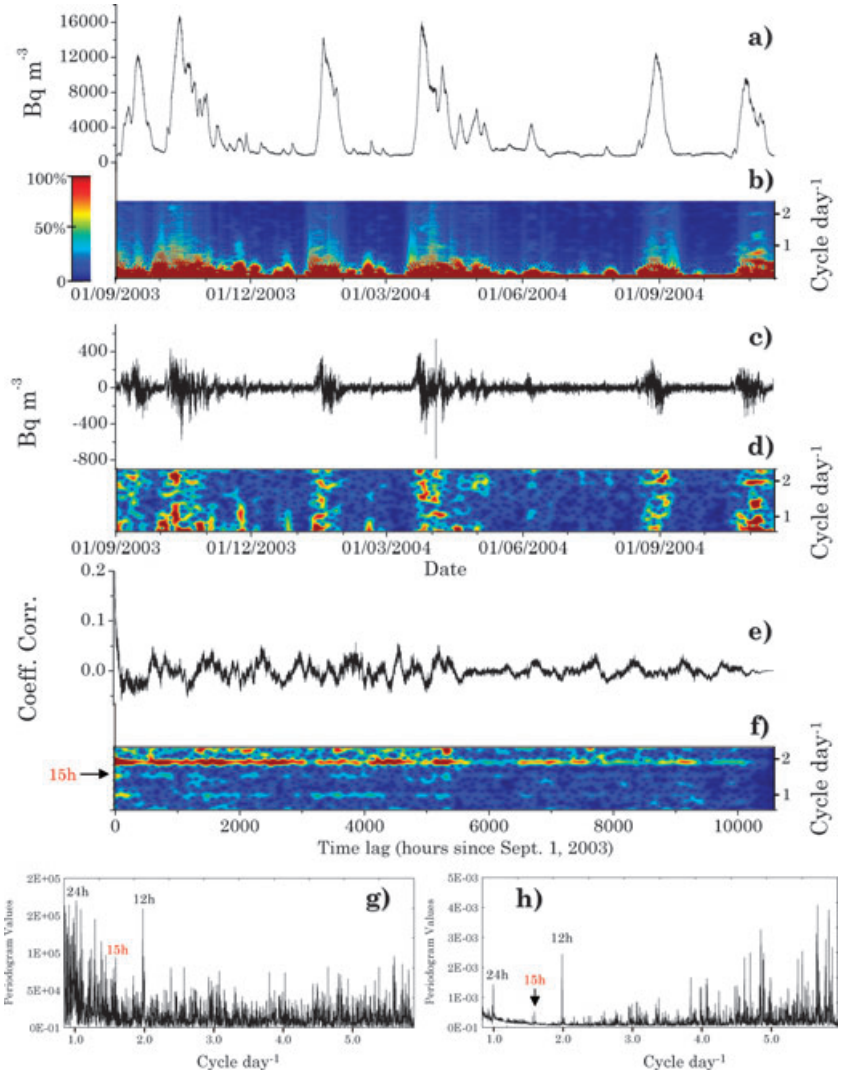

Figure 8. Steps for a modified spectrogram analysis (MSA) using the hourly radon-222 signal (a) in the tunnel atmosphere during Period 1 (see Fig. 3) from 2003 September 1 to 2004 November 16. A synthetic signal with a 15 hr period and 10 Bq m^{-3} peak-to-peak amplitude has been added to the raw AlphaGUARD^{TM} data to test this method and evaluate its sensitivity. To enhance periodicities not revealed by a normal spectrogram (b and d), we applied an autocorrelation function (e) on the derivative (c) from which a new spectrogram (f) is calculated. The latter reveals a clear S_2, and small S_1 periodicity. The validity of the treatment is revealed through the clear detection of the artificial signal (15 hr) by the modified spectrogram analysis (MSA) whose sensitivity is illustrated by a FFT (g) of the raw data (a) and a FFT (h) of the autocorrelation (e) of the derivative (c).

S_2 signal is too small to be recorded by the BMC, but is still large enough to be recorded by the AlphaGUARD^{TM}. The S_2 and S_1 lines have also been observed in one flow rate (fracture water), but not in the matrix water flow rate and not in the carbon dioxide signal.

Taking the presence of a dominating S_2 line over a S_1 line as a signature of some sensitivity to atmospheric pressure variation, we conclude that this sensitivity is revealed in the radon signal during the bursts, in the fracture water flow rate, and is spatially organized in the temperature signals. This remarkable organisation indicates the presence of an additional mechanism relating atmospheric pressure and temperature, possibly advective transport from the pore space to the tunnel atmosphere, with a reservoir located below the tunnel floor. The geothermal gradient, at the depth of the tunnel, has been measured in two nearby boreholes and is normal with a slope of about 0.8 °C per 100 m. Thus, barometric pumping from below the tunnel roof is expected to advect air hotter than the static tunnel air. Atmospheric pressure sensitivity during the bursts suggests a transport mechanism largely in the air phase of the unsaturated medium. The mechanism at the origin of the burst therefore must be accompanied by a large increase of the air permeability or fluid pressure in the rock mass in the vicinity of the tunnel. Similar result has been obtained from hydrogeochemistry by Pili *et al*. (2004).

The spectrogram as a function of time, and in particular the temporal variations of S_2 line, can therefore be used as an index of mixing of pore air with tunnel air. This mixing is remarkably observed directly during the largest radon burst of 2006 which also contains an episode of transient thermal inversion. Note that the S_1 line has a temporal variation more or less similar to the S_2. The fact that the S_2 periodicity dominates over the S_1 periodicity in the fracture water signal (Fig. 9c) suggests a sensitivity to atmospheric pressure, which is highly time dependent. The absolute value of flow rate does not seem to play a role.

Thus, a factor other than the flow rate itself must be controlling the S_1 and S_2 and, hence, the pressure sensitivity of the fracture water flow rate. Such a factor could be a low water content of some fractures, or the changes in connectivity between fractures and

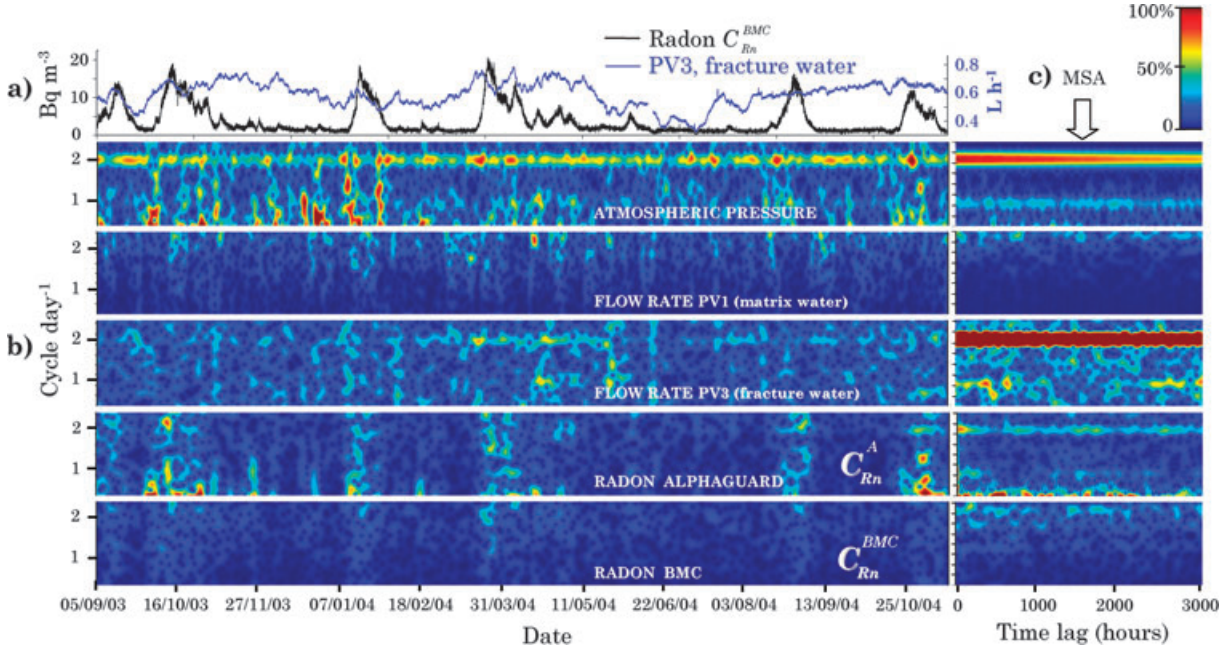

Figure 9. Spectral analysis of atmospheric pressure, matrix water PV1 and fracture water PV3 dripwater flow rates, radon measured by AlphaGUARD^{TM} and BMC in the Roselend tunnel during Period 1 (see Fig. 3). (a) Radon and fracture water time-series. (b) Classical spectrograms as a function of time. Barometric tide S_2 (with $S_2 > S_1$) appear only in atmospheric pressure and fracture water flow rate signals. (c) MSA applied to each parameter. A clear S_2 line appears for the atmospheric pressure, fracture water flow rate and radon-222 measured by AlphaGUARD^{TM}.

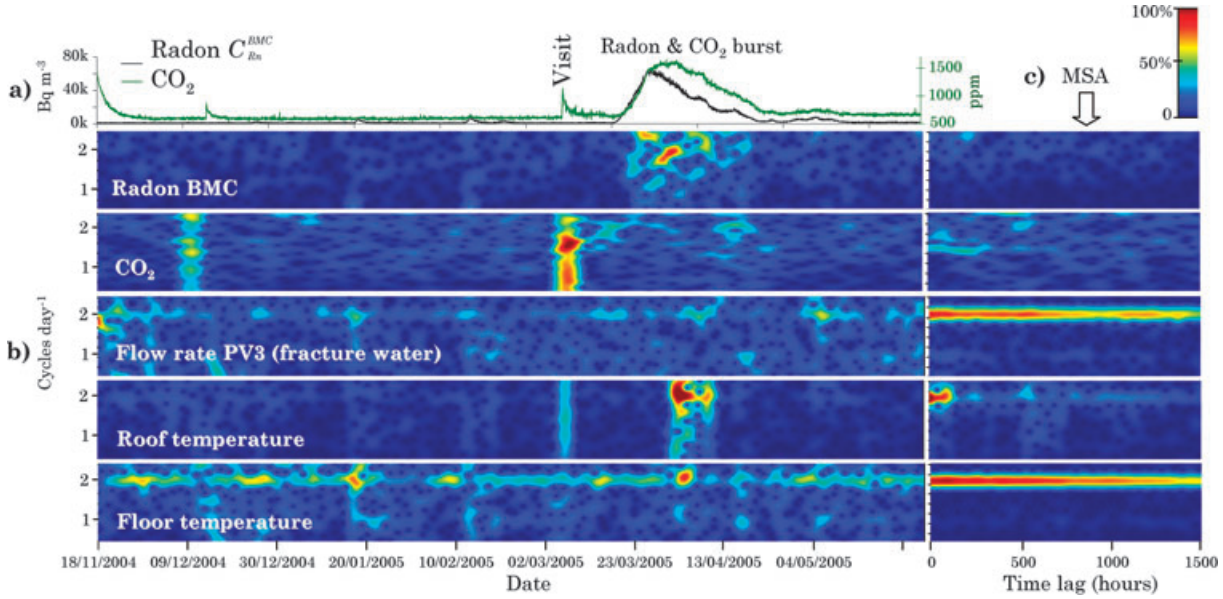

Figure 10. Spectral analysis of CO_2, radon (BMC), fracture water flow rate, floor and roof temperature in the Roselend tunnel during Period 2 (see Fig. 3). (a) Radon and CO_2 time-series. (b) Classical spectrograms as a function of time. (c) MSA applied to each parameter.

the porous matrix. In particular, the strongest S_2 line is observed from mid 2004 March to mid 2004 May (Fig. 9b), during the short period of emptying of the Roselend Lake (Fig. 3). This atmospheric pressure sensitivity of the flow rate that coincides with low lake levels is confirmed in 2003 and 2005. Such a relationship between the lake water level and the atmospheric pressure sensitivity is plausible. It can be linked to the interplay of matrix and fractures during deformation of the rock massif. Indeed, in a first approximation, one can represent the deformation induced by the loading and unloading of lake water as a vertical force applied on an elastic half space. The force equivalent to the lake water is located about 1 km from the tunnel. At the ground surface, the weight of water, at high water level, results in extension, whereas low water level corresponds to compression. At the scale of the deforming system, the tunnel is actually located near the ground surface. In the presence of compressive stress during an emptying of the lake, pore water from the matrix would be squeezed into the unsaturated fractures, from where drops of atmospheric pressure could enhance its flow into the tunnel. This intuitive analysis was confirmed by numerical elastic modelling (A.-S. Provost 2005, personal communication).

This would need further confirmation by a detailed poroelastic modelling.

By contrast with fracture water (PV3), no S_2 or S_1 line is evidenced in matrix water (PV1) neither from the MSA nor the spectrogram as a function of time. Using these tools, we can make a firmer statement than with the Fourier spectra of Fig. 6 that this flow rate shows no periodicity, and in particular no detectable sensitivity to atmospheric pressure variation. The evidenced sensitivity to barometric pressure (S_2) of dripwater flow rates contributed from fracture networks (PV3) is in agreement with the hydrogeochemical findings that fracture flow is connected to the surface in unsaturated conditions. Similarly, the absence of S_2 in dripwater flow rates contributed from the matrix water is in agreement with flow in saturated conditions and disconnected from the surface.

This study suggests that, while the fracture water flow rate exhibits an interesting sensitive temporal pattern, it does not seem directly related to the radon bursts. If the radon bursts have a relationship with groundwater circulation, therefore, they are not due to dripwater from above, but they must be generated from below. In addition, we see that, while we have for the first time, reported carbon dioxide bursts simultaneously with the largest radon bursts, the S_2 line was not observed in this signal. In addition, carbon dioxide release seems to appear with some time delay and with smaller relative intensity than the radon bursts. The radon bursts remain an unusual and spectacularly amplified response of the tunnel.

6 CONCLUSION

In this paper, we show that periodicities can be difficult to extract in time-series describing physical systems, but that their presence brings important indication on the underlying processes. Once the periodicities are observed, it is useful to monitor their intensity as a function of time. For this purpose, we show the results of various spectrogram methods. In general, it is interesting to compare different methods, and in particular to combine methods that can evidence the presence of the periodicities, such as the MSA, and methods that can provide information as a function of time. In the case of the Roselend tunnel, we show that the S_2 wave, sometimes difficult to observe, exhibits both slow temporal variations at time scales of several months (fracture water signal, PV3 in Fig. 9) and transient variations with times scales from a few days to a few weeks (radon time-series in Fig. 8).

It is interesting to perform such analysis prior to undertaking a detailed modelling because the study of periodicities provides information on the underlying physical processes, which can be, as in the Roselend tunnel, complex and time dependent. In this case, indeed, the examination of periodicities sheds some light on the mechanism producing transient bursts of radon and carbon dioxide. The S_2 periodicity of the radon signal, interpreted as a proxy for atmospheric pressure sensitivity in the absence of large daily variations, suggests a mechanism taking place in unsaturated host rock, likely to be driven by fracture fluids. By contrast, the lack of the S_2 line in the carbon dioxide suggests a transport in the water phase. Since no significant water dripping is observed during the bursts, groundwater must be released in the tunnel from below.

The following scenario, thus, can be proposed: in response to some hydromechanical effect, groundwater from some reservoir located below the tunnel is moved upwards, pushing some radon-rich pore air into the tunnel, and simultaneously, pore water. Carbon dioxide, primarily contained in this pore water, is subsequently slowly degassed into the tunnel atmosphere, accounting for the delayed maximum concentration. A detailed quantitative model can now be worked out to account for all data, including additional data from nearby boreholes.

The methods and analysis of periodicities presented here can be applied to other physical systems, such as painted caves or underground waste storage. Indeed, the analysis and monitoring of periodicities appears as a powerful tool to characterize porous fracture media, through barometric pumping via the S_2 wave, or other periodical forcings. Daily variations provide another observable, which may reflect temperature induced ventilation processes (Perrier *et al.* 2007). The earth tide is another periodical signal in the same frequency range, which may be very important to study and monitor as an indicator of mechanical sensitivity. All these forcings are present simultaneously, but their size and temporal variations can be different in various observables. For this purpose, it is important to monitor both parameters sensitive to the pore air phase, such as radon concentration, and parameters sensitive to fracture or matrix water, such as flow rates.

To make progress, it appears fruitful to maintain a sufficient number of instruments over several years in more physical systems, in particular underground sites which provide more stability, but also on other sites such as active faults or volcanoes. The acquisition of long data series in different conditions and their thorough examinations, will shed light on the complex dynamics of natural systems, with the hope to provide a meaningful understanding and the possibility of predicting long term and transient phenomena.

ACKNOWLEDGMENTS

The authors thank Electricité de France (EDF) for its water level data and access to the lake and the city of Beaufort (Savoie, France) for the access to the Roselend tunnel. The experiments have been performed thanks to the enthusiastic and thoughtful collaboration of Pr. Osam Sano, Sarah Bureau, Ann-Sophie Provost, Isabelle Jeannin, Delphine Patriarche, and thanks to the technical help of Patrick Carrera and Bertrand Menotto. This is IPGP contribution 2436.

REFERENCES

Arabelos, D.N., Asteriadis, G., Contadakis, M.E., Spatalas, S.D. & Sachsamanoglou, H., 1997. Atmospheric tide in the area of Tessaloniki, *J. Geodyn.,* **23,** 65–75.

Baubron, J.-C., Allard, P., Sabroux, J.-C., Tedesco, D. & Toutain, J.-P., 1991. Soil gas emanations as precursory indicators of volcanic eruptions, *J. Geol. Soc. (Lond.),* **148,** 571–576.

Box, G.E.P. & Jenkins, G., 1976. *Time Series Analysis: Forecasting and Control,* revised ed., Holden-Day, San Francisco, CA, 575p.

Cigolini, C., Gervino, G., Bonetti, R., Conte, F., Laiolo, M. & Coppola, D., 2005. Tracking precursors and degassing by radon monitoring during major eruptions at Stromboli Volcano (Aeolian Islands, Italy), *Geophys. Res. Lett.,* **32,** L12308.

Clements, W.E. & Wilkening, M.H., 1974. Atmospheric pressure effects on ^{222}Rn transport across the earth-air interface, *J. geophys. Res.,* **79,** 5025–5029.

Crockett, R.G.M., Gillmore, G.K., Phillips, P.S., Denman, A.R. & Groves-Kirkby, C.J., 2006a. Radon anomalies preceding earthquakes which occurred in the UK, in summer and autumn 2002, *Sci. Total Environ.,* **364,** 138–148.

Crockett, R.G.M., Gillmore, G.K., Phillips, P.S., Denman, A.R. & Groves-Kirkby, C.J., 2006b. Tidal synchronicity of built-environment radon levels in the UK, *Geophys. Res. Lett.,* **33,** L05308, doi:05310.01029/02005GL024950.

Crouzeix, C., Le Mouël, J.-L., Perrier, F. & Richon, P., 2006. Thermal stratification induced by heating in a non-adiabatic context, *Build. Environ.,* **41,** 926–939.

Genty, D. & Deflandre, G., 1998. Drip flow variations under a stalactite of the Père Noël cave (Belgium). Evidence of seasonal variations and air pressure constraints, *J. Hydrol.,* **211,** 208–232.

Haurwitz, B. (Ed.) 1956. *The Geographical Distribution of the Solar Semidiurnal Pressure Oscillation,* 36 pp., College of Engineering, New York University.

Haurwitz, B. & Cowley, A.D., 1973. The diurnal and semidiurnal barometric oscillations, global distribution and annual variation, *Pure appl. Geophys.,* **102,** 193–222.

Holub, R.F. & Brady, B.T., 1981. The effect of stress on radon emanation from rock, *J. geophys. Res.,* **86,** 1776–1784.

Ielsch, G. *et al*., 2001. Radon (^{222}Rn) level variations on a regional scale: influence of the basement trace element (U, Th) geochemistry on radon exhalation rates, *J. Environ. Radioact.,* **53,** 75–90.

Igarashi, G., Saeki, S., Takahata, N., Sumikawa, K., Tasaka, S., Sasaki, Y., Takahashi, M. & Sano, Y., 1995. Ground-water radon anomaly before the Kobe earthquake in Japan, *Science,* **269,** 60–61.

Khinchin, A.I. (Ed.) 1949. *Mathematical Foundations of Statistical Mechanics,* 179 pp., Dover Publications, Inc., New York, NY.

King, C.-Y. & Guangwei, L., 1990. Variations of electric resistance and H_2 and Rn emissions of concrete blocks under increasing uniaxial compression, *Pure appl. Geophys.,* **134,** 45–56.

Lehmann, B.E., Lehmann, M., Neftel, A. & Tarakanov, S.V., 2000. Radon-222 monitoring of soil diffusivity, *Geophys. Res. Lett.,* **27,** 3917–3920.

Martín-Luis, C., Quesada, M., Eff-Darwich, A., De la Nuez, J., Coello, J., Ahijado, A., Casillas, R. & Soler, V., 2002. A new strategy to measure radon in an active volcanic island (Tenerife, Canary Islands), *Environ. Geol.,* **43,** 72–78.

Nazaroff, W.W., 1992. Radon transport from soil to air, *Rev. Geophys.,* **30,** 137–160.

Olvera, F.E., 2005. A spectral analysis of the sunspot time series using the periodogram, 4 pp, PSU Electrical & Computer Engineering, ECE 5/638: Fall 2005.

Papastefanou, C., 2002. An overview of instrumentation for measuring radon in soil gas and groundwaters, *J. Environ. Radioact.,* **63,** 271–283.

Patriarche, D., Pili, E., Adler, P.M. & Thovert, J.-F., 2007. Stereological analysis of fractures in the Roselend tunnel and permeability determination, *Water Resour. Res.,* **43,** W09421.

Perrier, F., Morat, P. & Le Mouël, J.-L., 2001. Pressure induced temperature variations in an underground quarry, *Earth planet. Sci. Lett.,* **191,** 145–156.

Perrier, F., Richon, P., Crouzeix, C., Morat, P. & Le Mouël, J.-L., 2004. Radon-222 signatures of natural ventilation regimes in an underground quarry, *J. Environ. Radioact.,* **71,** 17–32.

Perrier, F., Le Mouël, J.L., Poirier, J.P. & Shnirman, M.G., 2005a. Long-term climate change and surface versus underground temperature measurements in Paris, *Int. J. Clim.,* **25,** 1619–1631.

Perrier, F., Richon, P. & Sabroux, J.-C., 2005b. Modelling the effect of air exchange on ^{222}Rn and its progeny concentration in a tunnel atmosphere, *Sci. Total Environ.,* **350,** 136–150.

Perrier, F., Richon, P., Gautamd, U., Tiwarid, D.R., Shresthad, P. & Sapkotad, S.N., 2007. Seasonal variations of natural ventilation and radon-222 exhalation in a slightly rising dead-end tunnel, *J. Environ. Radioact.,* **97,** 220–235.

Pili, E., Perrier, F. & Richon, P., 2004. Dual porosity mechanism for transient groundwater and gas anomalies induced by external forcing, *Earth planet. Sci. Lett.,* **227,** 473–480.

Pili, E., Bureau, S., Perrier, F., Patriarche, D., Charlet, L., Adler, P.M. & Richon, P., 2008. Reactive transport and residence times in unsaturated fractured rocks from field-scale experiments, in *Adsorption of Metals by Geomedia II, Developments in Earth & Environmental Sciences,* pp. 445–473, eds M. Barnett and D. Kent, Elsevier, Amsterdam.

Pinault, J.-L. & Baubron, J.-C., 1997. Signal processing of diurnal and semidiurnal variations in radon and atmospheric pressure: a new tool for accurate in situ measurement of soil gas velocity, pressure gradient, and tortuosity, *J. geophys. Res.,* **102,** 18101–18120.

Pohl-Rüling, J. & Pohl, E., 1969. The Radon-222 concentration in the atmospheres of mines as a function of the barometric pressure, *Health Phys.,* **16,** 579–584.

Porstendörfer, J., 1996. Radon: measurements related to dose, *Environ. Int.,* **22,** 563–583.

Provost, A.-S., Richon, P., Pili, E., Perrier, F. & Bureau, S., 2004. Fractured porous media under influence: the Roselend experiment, *EOS,* **85,** 113–124.

Ray, R.D., 2001. Comparisons of global analyses and station observations of the S_2 barometric tide, *J. Atmos. Sol.-Terr. Phys.,* **63,** 1085–1097.

Richon, P., Sabroux, J.-C., Halbwachs, M., Vandemeulebrouck, J., Poussielgue, N., Tabbagh, J. & Punongbayan, R., 2003. Radon anomaly in the soil of Taal volcano, the Philippines: a likely precursor of the M 7.1 Mindoro earthquake (1994), *Geophys. Res. Lett.,* **30,** 1481.

Richon, P., Perrier, F., Sabroux, J.-C., Trique, M., Ferry, C., Voisin, V. & Pili, E., 2004. Spatial and time variations of radon-222 concentration in the atmosphere of a dead-end horizontal tunnel, *J. Environ. Radioact.,* **78,** 179–198.

Ruckerbauer, F. & Winkler, R., 2001. Radon concentration in soil gas: a comparison of methods, *Appl. Radiat. Isot.,* **55,** 273–280.

Simpson, G.C., 1919. The twelve-hourly barometer oscillation, *Q. J. R. Meteorol. Soc.,* **44,** 1–18.

Tanner, A.B., 1964. Radon migration in the ground: a review, *Paper Presented at The Natural Radiation Environment,* Chicago Univ. Press, Chicago.

Trique, M., Richon, P., Perrier, F., Avouac, J.-P. & Sabroux, J.-C., 1999. Radon emanation and electric potential variations associated with transient deformation near reservoir lakes, *Nature,* **399,** 137–141.

Unger, A., Finsterle, S. & Bodvarsson, G., 2004. Transport of radon gas into a tunnel at Yucca Mountain—estimating large-scale fractured tuff hydraulic properties and implications for the operation of the ventilation system, *J. Contam. Hydrol.,* **70,** 153–171.

Virk, H.S. & Singh, B., 1994. Radon recording of Uttarkashi earthquake, *Geophys. Res. Lett.,* **21,** 737–740.

Yamauchi, T. & Shimo, M., 1982. Radon concentration in galleries and its relation to the earthquake occurrence, *J. Seismol. Soc. Jpn,* **35,** 435–446.

Yasuoka, Y. & Shinogi, M., 1997. Anomaly in atmospheric radon concentration: a possible precursor of the 1995 Kobe, Japan, earthquake, *Health Phys.,* **72,** 759–761.